

Linear-in temperature resistivity from an isotropic Planckian scattering rate

<https://doi.org/10.1038/s41586-021-03697-8>

Received: 25 November 2020

Accepted: 3 June 2021

Published online: 28 July 2021

 Check for updates

Gaël Grissonnanche^{1,2,3}, Yawen Fang², Anaëlle Legros^{1,4}, Simon Verret¹, Francis Laliberté¹, Clément Collignon¹, Jianshi Zhou⁵, David Graf⁶, Paul A. Goddard⁷, Louis Taillefer^{1,8}✉ & B. J. Ramshaw^{2,8}✉

A variety of ‘strange metals’ exhibit resistivity that decreases linearly with temperature as the temperature decreases to zero^{1–3}, in contrast to conventional metals where resistivity decreases quadratically with temperature. This linear-in-temperature resistivity has been attributed to charge carriers scattering at a rate given by $\hbar/\tau = \alpha k_B T$, where α is a constant of order unity, \hbar is the Planck constant and k_B is the Boltzmann constant. This simple relationship between the scattering rate and temperature is observed across a wide variety of materials, suggesting a fundamental upper limit on scattering—the ‘Planckian limit’^{4,5}—but little is known about the underlying origins of this limit. Here we report a measurement of the angle-dependent magnetoresistance of $\text{La}_{1.6-x}\text{Nd}_{0.4}\text{Sr}_x\text{CuO}_4$ —a hole-doped cuprate that shows linear-in-temperature resistivity down to the lowest measured temperatures⁶. The angle-dependent magnetoresistance shows a well defined Fermi surface that agrees quantitatively with angle-resolved photoemission spectroscopy measurements⁷ and reveals a linear-in-temperature scattering rate that saturates at the Planckian limit, namely $\alpha = 1.2 \pm 0.4$. Remarkably, we find that this Planckian scattering rate is isotropic, that is, it is independent of direction, in contrast to expectations from ‘hotspot’ models^{8,9}. Our findings suggest that linear-in-temperature resistivity in strange metals emerges from a momentum-independent inelastic scattering rate that reaches the Planckian limit.

Immediately following the discovery of high-temperature superconductivity in the cuprates, it was noted that their normal-state resistivity is linear over a broad temperature range¹⁰. Linear-in temperature (T -linear) resistivity extending to low temperatures indicates a strongly correlated metallic state, and it was recognized early on that understanding T -linear resistivity may be the key to unravelling the mystery of high-temperature superconductivity itself¹¹. Since then, T -linear resistivity has become a widespread phenomenon in strongly correlated metals, occurring in systems as diverse as organic and iron-based superconductors³ and magic-angle twisted bilayer graphene¹². The fact that T -linear resistivity is often found in proximity to unconventional superconductivity is highly suggestive of a common underlying origin, but T -linear resistivity at low temperatures lies outside the standard Fermi-liquid description of metals and thus remains a central unsolved problem in quantum materials research.

The difficulty in developing a controlled, microscopic theory of T -linear resistivity has led to the creation of new theoretical approaches that draw on techniques developed for the study of quantum gravity, including holography and the Sachdev–Ye–Kitaev model^{13–17}. Although these theories are not microscopically motivated, they explicitly account for strong quasiparticle interactions in a controlled way and suggest that T -linear resistivity might emerge

as a universal principle—independent of microscopic details. The transport scattering rate $1/\tau$ in these models obeys the so-called Planckian limit:

$$\frac{\hbar}{\tau} = \alpha k_B T, \quad (1)$$

where k_B and \hbar are the Boltzmann and Planck constants, respectively, and α is a constant of order unity. Simple estimates of α , based on the Drude model, from a wide variety of metals with T -linear resistivity are consistent with Planckian-limit scattering^{4,5,18}. The Planckian limit even applies to conventional metals such as gold and copper, where T -linear resistivity at high temperatures is caused by electron–phonon scattering. Phonons, however, cannot explain T -linear resistivity in the $T \rightarrow 0$ limit, suggesting that the Planckian limit is independent of microscopic origin. Estimates based on the Drude model provide no information about how the scattering rate varies in momentum space. Angle-resolved photoemission spectroscopy (ARPES) does provide the momentum dependence¹⁹, but only for the single-particle scattering rate and not for the transport scattering rate that determines the resistivity. What has been missing is a full momentum-space description of the transport scattering rate.

¹Département de physique, Institut quantique, RQMP, Université de Sherbrooke, Sherbrooke, Québec, Canada. ²Laboratory of Atomic and Solid State Physics, Cornell University, Ithaca, NY, USA.

³Kavli Institute at Cornell for Nanoscale Science, Ithaca, NY, USA. ⁴SPEC, CEA, CNRS-UMR 3680, Université Paris-Saclay, Gif-sur-Yvette, France. ⁵Materials Science and Engineering Program, Department of Mechanical Engineering, University of Texas at Austin, Austin, TX, USA. ⁶National High Magnetic Field Laboratory, Tallahassee, FL, USA. ⁷Department of Physics, University of Warwick, Coventry, UK. ⁸Canadian Institute for Advanced Research, Toronto, Ontario, Canada. ✉e-mail: louis.taillefer@usherbrooke.ca; bradramshaw@cornell.edu

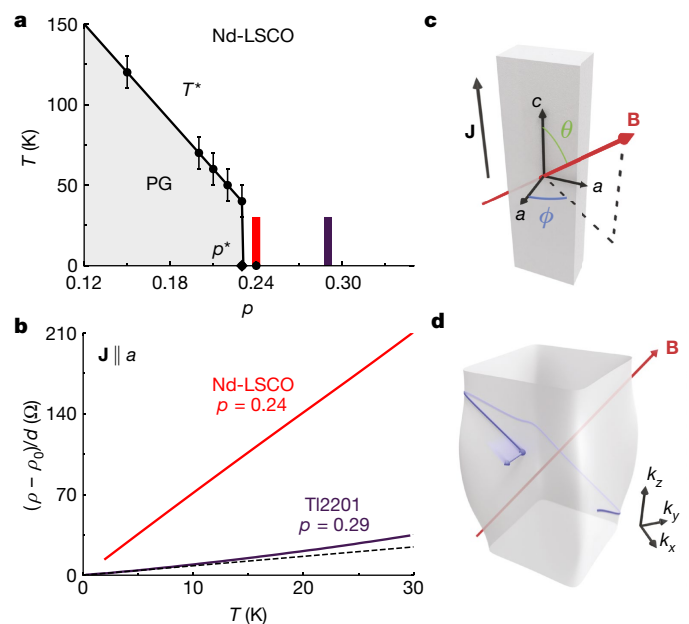


Fig. 1 | T-linear resistivity and the angle-dependent magnetoresistance technique. **a**, Temperature-doping phase diagram of the hole-doped cuprate Nd-LSCO. The pseudogap phase (PG), which onsets below a critical doping of $p^* = 0.23$ in Nd-LSCO, is highlighted in grey (the onset temperature T^* of the pseudogap phase is taken from refs.^{6,20} and defined as an upturn in the resistivity. The error bars, taken from ref.⁶, reflect the uncertainty in pinpointing that upturn). The superconducting dome is not represented as it can be suppressed with a magnetic field $B \parallel c \geq 20$ T. The red stripe indicates Nd-LSCO at $p = 0.24$ measured in the ADMR experiment and the violet stripe represents Tl2201 at $p = 0.29$. **b**, In-plane resistivity per copper-oxide plane as a function of temperature for Nd-LSCO at $p = 0.24$ at $B = 35$ T (ref.⁶; red) and Tl2201 at $p = 0.29$ at $B = 13$ T (ref.³⁷; violet). For both sets of data, the elastic part of the resistivity ρ_0 has been subtracted from the total resistivity $\rho(\rho_{xx})$ and divided by the distance d between the CuO_2 planes. The black dashed line is the T -linear component of the resistivity of Tl2201 $p = 0.29$. **c**, Geometry of the ADMR measurement. The sample is represented in grey. The black arrow on the left identifies the direction of the electric current, \mathbf{J} , along the c axis. The angles ϕ and θ describe the direction of the magnetic field \mathbf{B} with respect to the crystallographic a and c axes. **d**, The three-dimensional Fermi surface of Nd-LSCO at $p = 0.24$ obtained from the ADMR. A single cyclotron orbit, perpendicular to the magnetic field \mathbf{B} , is drawn in blue, with the Fermi velocity indicated with the small blue arrow at a particular instant in time.

Technique

To measure the transport scattering rate in a metal with T -linear resistivity, we turn to the high-temperature cuprate $\text{La}_{1.6-x}\text{Nd}_{0.4}\text{Sr}_x\text{CuO}_4$ (Nd-LSCO) at a hole doping of $p = 0.24$. Strange metals are often found in proximity to a quantum critical point and the pseudogap critical point in Nd-LSCO terminates at a hole doping of $p^* = 0.23$ as determined by both transport²⁰ and ARPES⁷ measurements (Fig. 1a). At $p = 0.24$, Nd-LSCO shows perfectly T -linear resistivity^{6,20} down to the lowest measured temperatures once superconductivity is suppressed by a magnetic field (Fig. 1b).

The technique we use to access the quasiparticle scattering rate is angle-dependent magnetoresistance (ADMR), which measures variations in the c -axis resistivity (ρ_{zz}) as the sample is rotated to different azimuthal (ϕ) and polar (θ) angles with respect to an external magnetic field \mathbf{B} (Fig. 1c). The intuitive way of understanding ADMR is to consider that resistivity depends only on the lifetimes and velocities of quasiparticles at the Fermi surface. The application of a magnetic field alters quasiparticle velocities through the Lorentz force, producing variations in the c -axis resistivity that depend sensitively on the direction of the

magnetic field, hence angle-dependent magnetoresistance. We compare the measured ADMR to calculations made using Chambers' exact solution to the Boltzmann transport equations in a magnetic field²¹ and adjust the Fermi surface geometry and the momentum dependence of the quasiparticle scattering rate in our model until the calculations match the experimental data. This procedure does not assume the presence of a Fermi liquid: Boltzmann transport has been shown to be valid even in cases where Fermi-liquid quasiparticles are not well defined^{22,23}.

Results

The left panels of Fig. 2a show the ADMR of Nd-LSCO at $p = 0.24$ for $T = 6$ K, $T = 12$ K, $T = 20$ K and $T = 25$ K. These measurements were performed at the National High Magnetic Field Laboratory using a single-axis rotator to vary the polar angle θ in a fixed field of 45 T (see Fig. 1c for the experimental geometry). We determine the Fermi surface geometry and the quasiparticle scattering rate by fitting the data simultaneously at all temperatures to a one-band tight-binding model that is commonly used for LSCO-based cuprates (Methods.) We optimize the tight-binding and scattering-rate parameters using a genetic algorithm, taking initial parameter estimates from previous ARPES measurements^{7,24}. We set the overall energy scale of the model to be $t = 160 \pm 30$ meV based on the measured specific heat²⁵ (Methods). Note that, below 10 K, the specific heat of Nd-LSCO at $p = 0.24$ increases as $\log(1/T)$ as $T \rightarrow 0$. The resistivity, however, remains linear to low temperature, suggesting that either this correction renormalizes the scattering rate and the bandwidth equally and thus cancels, or the $\log(1/T)$ factor is not associated with the conduction electrons. As our measurements cannot distinguish between these two scenarios, we omit the $\log(1/T)$ factor (which would reduce the bandwidth by about 20% at 6 K; Methods).

The simulated ADMR curves produced by these fits are shown in the right panels of Fig. 2a. Key features reproduced by the fit include the position of the maximum near $\theta = 40^\circ$, the onset of ϕ dependence beyond $\theta = 30^\circ$, the ϕ -dependent peak/dip near $\theta = 90^\circ$ and the absolute value of ρ_{zz} . The Fermi surface produced by this fit, shown in Fig. 1d, agrees with ARPES measurements^{7,24}. The best-fit tight-binding parameters are the same as those determined by ARPES to within our uncertainty (Extended Data Table 1), demonstrating remarkable consistency between the two techniques.

We now consider the scattering rate obtained from the fit. We separate the scattering rate in our model into two components—one isotropic and one anisotropic: $1/\tau(\mathbf{k}) = 1/\tau_{\text{iso}} + 1/\tau_{\text{aniso}}(\mathbf{k})$ (where \mathbf{k} is the quasiparticle momentum). We find that the ADMR is best described by a highly anisotropic scattering rate that is largest near the 'anti-nodal' ($\phi = 0^\circ, \phi = 90^\circ, \phi = 180^\circ$ and $\phi = 270^\circ$) regions of the Brillouin zone and smallest near the 'nodal' ($\phi = 45^\circ, \phi = 135^\circ, \phi = 225^\circ$ and $\phi = 315^\circ$) regions (Fig. 2b). In Extended Data Fig. 3, we show that three different phenomenological models of $1/\tau(\mathbf{k})$ all converge to the same shape as a function of ϕ , indicating that our fit is independent of the specific function chosen (Fig. 2b).

We extract the scattering rate at each temperature by fitting the full θ - and ϕ -dependent ρ_{zz} , and we a priori assume no particular temperature dependence—the scattering-rate parameters are determined independently at each temperature, while the Fermi surface geometry parameters are held constant. We extract the temperature dependence of both the isotropic and anisotropic components of the quasiparticle scattering rate from these fits, shown in Fig. 2c. Remarkably, we find that the anisotropic scattering rate is temperature independent, while the isotropic scattering rate is linear in temperature.

To check the validity of these scattering rates, we use our fit parameters and Boltzmann transport to calculate the temperature dependence of ρ_{xx} and the Hall coefficient $R_{\text{H}} \equiv \rho_{xy}/B$ (where ρ_{xx} and ρ_{xy} are the longitudinal and transverse in-plane resistivities, respectively). We reproduce the temperature dependence of all three transport coefficients, as shown in Fig. 3. Although the Fermi surface at $p = 0.24$ is

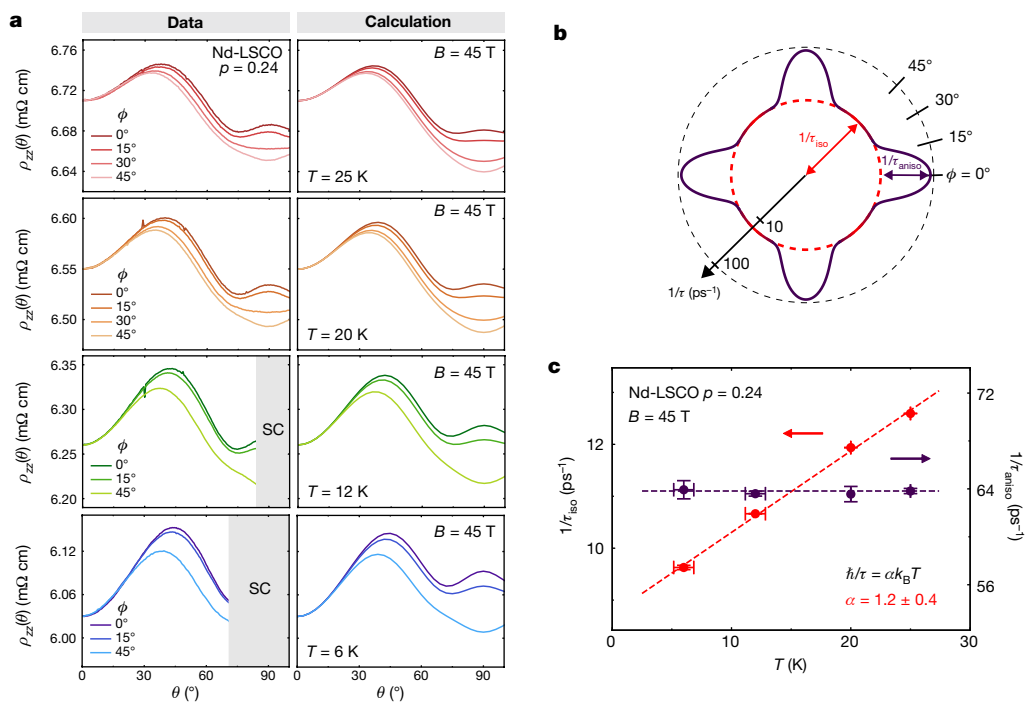


Fig. 2 | ADMR and quasiparticle scattering rate of Nd-LSCO at $p = 0.24$.
a, Left: the ADMR of Nd-LSCO at $p = 0.24$ as a function of θ for four different temperatures, $T = 25$ K, $T = 20$ K, $T = 12$ K and 6 K, and at $B = 45$ T. The grey area near $\theta = 90^\circ$ for $T = 6$ K and $T = 12$ K indicates the region where the sample becomes superconducting (SC). Right: simulations obtained from the Chambers formula using the tight-binding parameters of Extended Data Table 1 and the scattering-rate model of equation (7). **b**, Log-scale polar plot of the scattering rate at $T = 25$ K. Note the large scattering rate near the anti-nodes where the Fermi surface passes close to the van Hove point. The isotropic part of the scattering rate, $1/\tau_{\text{iso}}$, is shown as a dashed red line. The anisotropic part,

electron-like (that is, it is centred on the Γ point in the first Brillouin zone), both the measured and calculated R_H are hole-like due to the Fermi surface curvature²⁶ (Fig. 3b). An anisotropic scattering rate, highly enhanced near the anti-nodal regions of the Fermi surface (Figs. 2b, 3), is therefore not only required to correctly model the ADMR but also required to obtain the correct sign and magnitude of the Hall coefficient. To ensure that our fits are not fine-tuned for $B = 45$ T, we fit a second dataset taken at $B = 35$ T (Extended Data Fig. 5). We fix the tight-binding parameters to those obtained from the 45-T fits and we find that the same scattering-rate parameters emerge at 35 T, demonstrating the consistency of the model.

Discussion

We have measured the momentum dependence of the scattering rate responsible for the T -linear resistivity of Nd-LSCO at $p = 0.24$. We can write the total scattering rate as a sum of an elastic (temperature independent) component plus an inelastic (temperature dependent) component:

$$1/\tau(\phi, T) = 1/\tau_{\text{elastic}} + 1/\tau_{\text{inelastic}}(T). \quad (2)$$

We use the working definitions of ‘elastic scattering’ to mean temperature-independent scattering and ‘inelastic scattering’ to mean temperature-dependent scattering. There are exceptions to these definitions but they hold under most cases, particularly in the low-temperature limit. We find that $1/\tau_{\text{elastic}} = 1/\tau_{\text{aniso}}(\phi) + 1/\tau_{\text{iso}}(T = 0)$, that is, the elastic scattering contains all of the anisotropic scattering,

$1/\tau_{\text{aniso}}$ is shown in violet. The total scattering rate, $1/\tau_{\text{aniso}} + 1/\tau_{\text{iso}}$ is the entire solid line, shaded red or violet depending on whether it is dominated by $1/\tau_{\text{aniso}}$ or $1/\tau_{\text{iso}}$, respectively. **c**, Temperature dependence of the two components of the scattering rate. A linear fit to $1/\tau_{\text{iso}}$ using $1/\tau = A + \alpha k_B T/h$, yields $\alpha = 1.2 \pm 0.4$, a value consistent with the Planckian limit ($\alpha = 1$). The error bar on α accounts for the uncertainty in the fit as well as a $\pm 10\%$ uncertainty in the distance between the electrical contacts on the ADMR sample. By contrast, $1/\tau_{\text{aniso}}$ is seen to be temperature independent, showing that it comes entirely from elastic scattering off defects and impurities.

plus the $T = 0$ offset from the isotropic scattering. The elastic term is, by definition, temperature independent, and its angle dependence resembles the strongly ϕ -dependent density of states at $p = 0.24$ (Fig. 4c, e). It was previously suggested that similar anisotropy in the single-particle scattering rate (that is, the scattering rate measured by ARPES) may arise due to the proximity of the anti-nodal Fermi surface to the van Hove singularity²⁷. Our data suggest that similar anisotropy extends to the two-particle, transport scattering rate. Indeed, the momentum dependence of the elastic scattering rate we measure is reminiscent of the elastic scattering rate extracted by ARPES in LSCO at $p = 0.23$ (ref. 28), as shown in Supplementary Fig. 2.

We find that the inelastic term in equation (2) has a pure T -linear dependence whose strength is consistent with Planckian dissipation, that is, $1/\tau_{\text{inelastic}}(T) = \alpha \frac{k_B T}{h}$, with α close to 1 (Fig. 4f). This unambiguously demonstrates that T -linear resistivity is caused by a T -linear scattering rate and not, for example, by a T -dependent carrier density²⁹. Remarkably, we discover that this Planckian scattering is isotropic—the same for all directions of electron motion. Isotropic, T -linear scattering has been hypothesized in the context of a marginal Fermi liquid description of the normal state of cuprates¹¹. The marginal Fermi liquid also hypothesizes an ω -linear scattering rate (where ω is the angular frequency), and this was observed by ARPES in LSCO¹⁹. The absence of momentum-space structure to the scattering rate implies that the microscopic mechanism of T -linear resistivity is length-scale invariant, that is, it does not depend on scattering from a particular wavevector, such as the fluctuations of a finite- q order parameter (where q is the ordering wavevector). The fact that the inelastic scattering rate appears to reach a limit dictated by Planck’s constant suggests that a

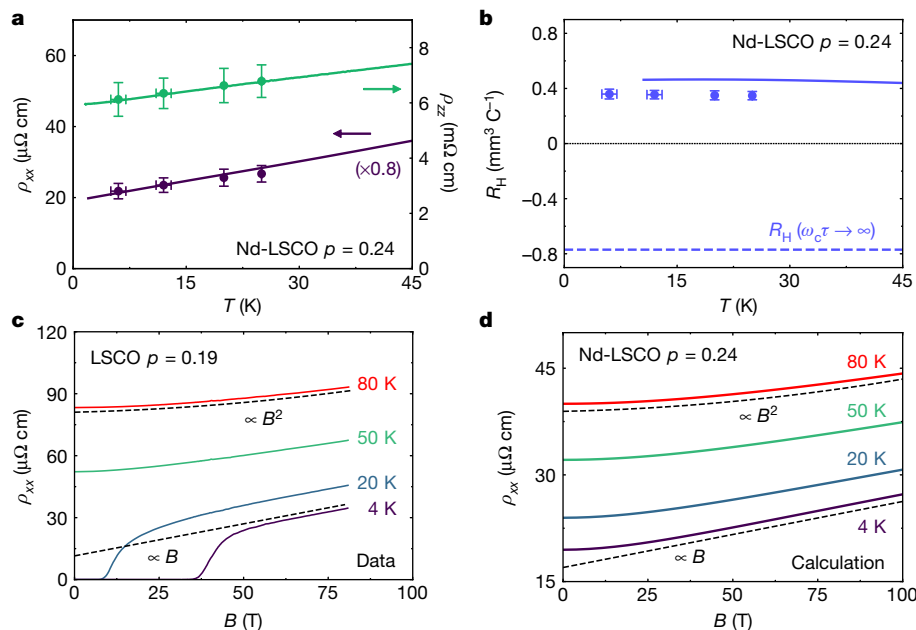


Fig. 3 | Transport coefficients of Nd-LSCO at $p = 0.24$. **a**, ρ_{xx} and ρ_{zz} at $B = 33$ T (**a**) and R_H at $B = 15$ T (**b**). Solid lines represent the data measured on Nd-LSCO at $p = 0.24$ (ρ_{xx} , ρ_{zz} and R_H , (ref. 4)). Circles represent the values calculated using the scattering rates plotted in Fig. 2c and the error bars are determined by the uncertainties in the fit parameters defined in Extended Data Tables 1 and 2. The ρ_{xx} data are taken on a different sample⁶ to that used in the AMDR measurements and from which the scattering rates are extracted. Although systematic errors on geometric factors are expected from sample to sample, it is seen that a constant factor of 0.8 on the data are sufficient to give excellent agreement between calculation and data. The dashed blue line in **b** represents the high-field ($\omega_c\tau \rightarrow \infty$) limit for the Fermi surface of Nd-LSCO at

$p = 0.24$. The difference between this limit and the data comes from the small value of $\omega_c\tau = 0.024$ at $T = 25$ K and $B = 45$ T and the fact that the conductivity is highest in the nodal directions where the Fermi surface has hole-like curvature (Fig. 4a). **c**, **d**, In-plane resistivity as a function of magnetic field, with data from LSCO at $p = 0.19$ (just above its own pseudogap critical point at $p^* = 0.18$)³¹ on the left and calculations using the scattering-rate values obtained from the AMDR data on Nd-LSCO at $p = 0.24$ (extrapolated linearly to 100 K) on the right. In our calculations, we find B -linear magnetoresistance at low temperature (dashed line) that becomes B^2 at high temperature (dashed line), as observed in LSCO $p = 0.19$.

fundamental quantum principle is at play, akin to that involved in the maximal rate of entropy production at a black hole event horizon³⁰. As was found in previous studies⁴, the Planckian limit constrains only the temperature-dependent part of the scattering rate.

Detailed knowledge of the Fermi surface and the scattering rate allows us to examine other transport properties in more quantitative detail than was previously possible. In Fig. 3d, we plot the calculated isotherms of ρ_{xx} versus B up to 100 T. We see that a strong B -linear component is present at low T above a threshold field, whereas a quadratic B^2 dependence dominates at high T and low B —strikingly similar to what was recently measured in LSCO³¹ (Fig. 3c). This B -linear magnetoresistance occurs naturally at intermediate fields between the low-field B^2 regime and the field-independent regime that occurs once $\omega_c\tau \gg 1$, where ω_c is the cyclotron frequency (ref. 32; see Supplementary Information for more details). When v_F , the Fermi velocity, or τ are highly anisotropic, as is the case for Nd-LSCO at $p = 0.24$ and LSCO at $p = 0.19$, the high-field regime is pushed up to extremely high fields, resulting in a broad region of B -linear magnetoresistance. This mechanism may explain B -linear magnetoresistance without any need for a B -dependent scattering rate. This is further supported by our fits to a second dataset taken at $B = 35$ T, which yield the same scattering rates we find at 45 T (Extended Data Fig. 5). It remains to be seen whether this mechanism can explain B -linear magnetoresistance more generally, for example, as found in iron pnictide superconductors³³, where the Fermi surface and scattering rate are unlikely to be as anisotropic as they are in Nd-LSCO.

In the context of our discovery that the inelastic scattering rate at p^* is both Planckian and isotropic, it is interesting to consider how this scattering rate evolves into the overdoped regime. Far above p^* , for

example in LSCO at $p = 0.33$ (ref. 34), the resistivity is T^2 as expected for a Fermi liquid. As the doping is lowered towards p^* , the T^2 component of the resistivity shrinks while a T -linear contribution grows³⁵. Previous AMDR studies on overdoped $Tl_2Ba_2CuO_{6+x}$ (Tl2201), at $p = 0.29$ (critical temperature $T_c = 15$ K)³⁶, have found coexistence between an isotropic T^2 scattering rate and an anisotropic T -linear scattering rate (Fig. 4d–f), agreeing with the temperature dependence of the resistivity in Tl2201 (Fig. 4b). Although AMDR has not been performed in a single material at both p^* and in the highly overdoped regime, a useful comparison can be made between Tl2201 and Nd-LSCO.

First, we compare the elastic scattering rate, which is isotropic in Tl2201 versus strongly anisotropic in Nd-LSCO (Fig. 4e). We attribute this to a difference in the density of states: nearly isotropic in Tl2201 (Fig. 4b, d) versus strongly anisotropic in Nd-LSCO due to the proximity of its Fermi surface to the van Hove point (Fig. 4a, c). The second, more interesting, difference between the two materials is in the inelastic scattering rate. In Nd-LSCO, the inelastic scattering rate is entirely T -linear and saturates the Planckian limit for all k directions (Fig. 4f). By contrast, the inelastic scattering in Tl2201 is only in part T -linear, and the magnitude of the T -linear component is only Planckian along the anti-nodal directions (Fig. 4f). As a result, the resistivity of Tl2201 is not T -linear, varying as $aT + bT^2$ (where a and b are temperature-independent coefficients), with a T -linear component one order of magnitude smaller than in Nd-LSCO (Fig. 1b). This comparison suggests that for a metal to display a pure T -linear resistivity, its scattering rate must grow to reach the Planckian limit for all directions. This could explain why a pure T -linear resistivity can be found in metals with vastly different Fermi surfaces, for example, quasi-one-dimensional single-band organic metals such as the Bechgaard salts³ and three-dimensional multiband

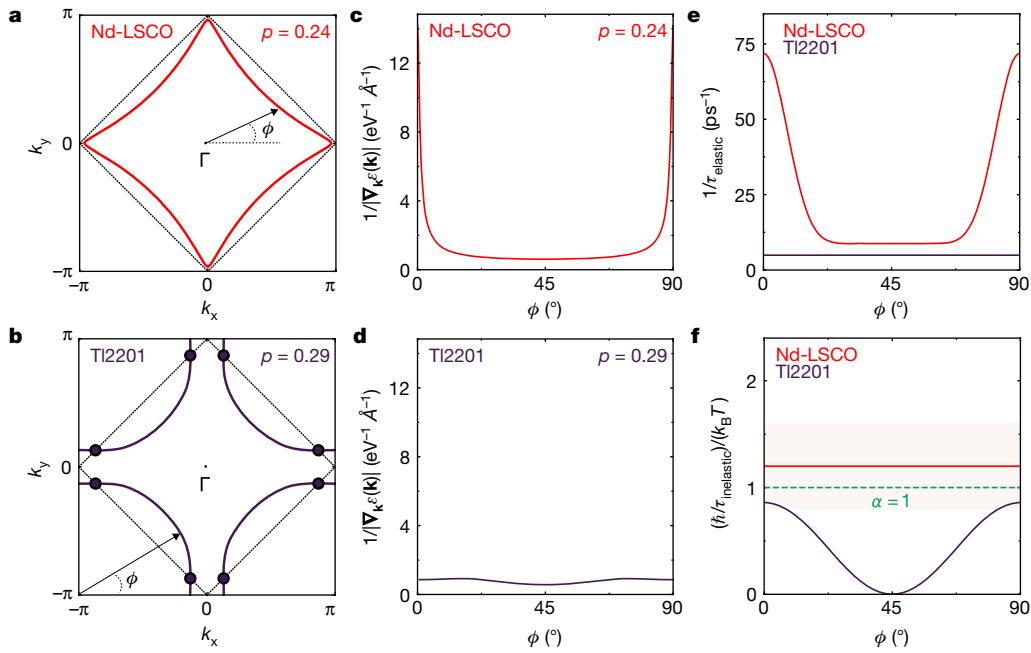


Fig. 4 | Comparison of two overdoped cuprates: Nd-LSCO and TI2201. **a, b**, Fermi surfaces at $k_z = \pi/c$ (where c is the c -axis lattice constant). In Nd-LSCO at $p = 0.24$ (**a**, red), the Fermi surface is electron-like and contained inside the antiferromagnetic zone boundary (black dotted lines). In TI2201, with $T_c = 15$ K (**b**, violet), the hole-like Fermi surface crosses the antiferromagnetic zone boundary at so-called hotspots (violet points). **c, d**, Density of states (DOS) $1/|\nabla_{\mathbf{k}}\epsilon(\mathbf{k})|$ as a function of the azimuthal angle ϕ , at $k_z = \pi/c$. In Nd-LSCO (**c**), the DoS is large at the antinodes due to proximity to the van Hove singularity. By contrast, in TI2201 (**d**), the DOS is nearly isotropic. **e**, Elastic part of the scattering rate versus azimuthal angle ϕ . In Nd-LSCO (**e**, red), the elastic scattering rate tracks the strong angle dependence of the DoS. By contrast, the

elastic scattering rate in TI2201 (violet; from ref. ³⁶) is isotropic, in accordance with the relatively isotropic DOS. **f**, Inelastic part of the scattering rate, multiplied by $\hbar/(k_B T)$, versus azimuthal angle ϕ . The inelastic scattering rate in Nd-LSCO is isotropic and consistent with ‘Planckian dissipation’ in the sense that $\hbar/\tau = \alpha k_B T$ with α of order 1 (the uncertainty in α is indicated by the red shading.) The inelastic T -linear scattering rate of TI2201 is strongly anisotropic, going from zero at $\phi = 45^\circ$ (nodal region) to a near-Planckian magnitude at $\phi = 0^\circ$ (anti-nodal region, near the hotspots). Note that in TI2201, there is also an isotropic T^2 part to the inelastic scattering rate, in addition to the anisotropic T -linear part shown here³⁶. This results in a resistivity that varies as $aT + bT^2$ (Fig. 1b)³⁷.

f -electron metals such as $\text{CeCu}_{5.9}\text{Au}_{0.1}$ (ref. ²). ADMR studies on TI2201 at lower doping would prove invaluable: we predict that the T -linear component of the scattering rate will grow in the nodal directions to become isotropic at p^* , while the T^2 component will decrease and then vanish at that same doping.

Online content

Any methods, additional references, Nature Research reporting summaries, source data, extended data, supplementary information, acknowledgements, peer review information; details of author contributions and competing interests; and statements of data and code availability are available at <https://doi.org/10.1038/s41586-021-03697-8>.

- Martin, S., Fiory, A. T., Fleming, R. M., Schneemeyer, L. F. & Waszczak, J. V. Normal-state transport properties of $\text{Bi}_{2-x}\text{Sr}_{2-y}\text{CuO}_{6+z}$ crystals. *Phys. Rev. B* **41**, 846–849 (1990).
- Löhneysen, H. V. et al. Non-Fermi-liquid behavior in a heavy-fermion alloy at a magnetic instability. *Phys. Rev. Lett.* **72**, 3262–3265 (1994).
- Doiron-Leyraud, N. et al. Correlation between linear resistivity and T_c in the Bechgaard salts and the pnictide superconductor $\text{Ba}(\text{Fe}_{1-x}\text{Co}_x)_2\text{As}_2$. *Phys. Rev. B* **80**, 214531 (2009).
- Bruin, J. A. N., Sakai, H., Perry, R. S. & Mackenzie, A. P. Similarity of scattering rates in metals showing T -linear resistivity. *Science* **339**, 804–807 (2013).
- Legros, A. et al. Universal T -linear resistivity and Planckian dissipation in overdoped cuprates. *Nat. Phys.* **15**, 142–147 (2019).
- Daou, R. et al. Linear temperature dependence of resistivity and change in the Fermi surface at the pseudogap critical point of a high- T_c superconductor. *Nat. Phys.* **5**, 31–34 (2009).
- Matt C. E. et al. Electron scattering, charge order, and pseudogap physics in $\text{La}_{1.6-x}\text{Nd}_{0.4}\text{Sr}_x\text{CuO}_2$: an angle-resolved photoemission spectroscopy study. *Phys. Rev. B* **92**, 134524 (2015).
- Hlubina, R. & Rice, T. M. Resistivity as a function of temperature for models with hot spots on the Fermi surface. *Phys. Rev. B* **51**, 9253–9260 (1995).

- Stojković, B. P. & Pines, D. Theory of the longitudinal and Hall conductivities of the cuprate superconductors. *Phys. Rev. B* **55**, 8576–8595 (1997).
- Gurvitch, M. & Fiory, A. T. Resistivity of $\text{La}_{1.825}\text{Sr}_{0.175}\text{CuO}_2$ and $\text{YBa}_2\text{Cu}_3\text{O}_7$ at 1100 K: absence of saturation and its implications. *Phys. Rev. Lett.* **59**, 1337–1340 (1987).
- Varma, C. M., Littlewood, P. B., Schmitt-Rink, S., Abrahams, E. & Ruckenstein, A. E. Phenomenology of the normal state of Cu-O high-temperature superconductors. *Phys. Rev. Lett.* **63**, 1996–1999 (1989).
- Cao, Y. et al. Strange metal in magic-angle graphene with near Planckian dissipation. *Phys. Rev. Lett.* **124**, 076801 (2020).
- Parcollet, O. & Georges, A. Non-Fermi-liquid regime of a doped Mott insulator. *Phys. Rev. B* **59**, 5341–5360 (1999).
- Davison, R. A., Schalm, K. & Zaenen, J. Holographic duality and the resistivity of strange metals. *Phys. Rev. B* **89**, 245116 (2014).
- Hartnoll, S. A. Theory of universal incoherent metallic transport. *Nat. Phys.* **11**, 54–61 (2015).
- Patel, A. A. & Sachdev, S. Theory of a Planckian metal. *Phys. Rev. Lett.* **123**, 066601 (2019).
- Cha, P., Wentzell, N., Parcollet, O., Georges, A. & Kim, E.-A. Linear resistivity and Sachdev-Ye-Kitaev (SYK) spin liquid behavior in a quantum critical metal with spin-1/2 fermions. *Proc. Natl Acad. Sci. USA* **117**, 18341–18346 (2020).
- Corson, J., Orenstein, J., Oh, S., O’Donnell, J. & Eckstein, J. N. Nodal quasiparticle lifetime in the superconducting state of $\text{Bi}_2\text{Sr}_2\text{CaCu}_2\text{O}_{8+z}$. *Phys. Rev. Lett.* **85**, 2569 (2000).
- Kaminski, A. et al. Momentum anisotropy of the scattering rate in cuprate superconductors. *Phys. Rev. B* **71**, 014517 (2005).
- Collignon, C. et al. Fermi-surface transformation across the pseudogap critical point of the cuprate superconductor $\text{La}_{1.6-x}\text{Nd}_x\text{Sr}_x\text{CuO}_2$. *Phys. Rev. B* **95**, 224517 (2017).
- Chambers, R. G. The kinetic formulation of conduction problems. *Proc. Phys. Soc. A* **65**, 458–459 (1952).
- Prange, R. E. & Kadanoff, L. P. Transport theory for electron-phonon interactions in metals. *Phys. Rev.* **134**, A566–A580 (1964).
- Abrahams, E. & Varma, C. M. Hall effect in the marginal Fermi liquid regime of high- T_c superconductors. *Phys. Rev. B* **68**, 094502 (2003).
- Horio, M. et al. Three-dimensional Fermi surface of overdoped La-based cuprates. *Phys. Rev. Lett.* **121**, 077004 (2018).
- Michon, B. et al. Thermodynamic signatures of quantum criticality in cuprate superconductors. *Nature* **567**, 218–222 (2019).
- Narduzzo, A. et al. Violation of the isotropic mean free path approximation for overdoped $\text{La}_{2-x}\text{Sr}_x\text{CuO}_2$. *Phys. Rev. B* **77**, 220502 (2008).

27. Abrahams, E. & Varma, C. M. What angle-resolved photoemission experiments tell about the microscopic theory for high-temperature superconductors. *Proc. Natl Acad. Sci. USA* **97**, 5714–5716 (2000).
28. Chang, J. et al. Anisotropic breakdown of Fermi liquid quasiparticle excitations in overdoped $\text{La}_{2-x}\text{Sr}_x\text{CuO}_4$. *Nat. Commun.* **4**, 2559 (2013).
29. Pelc, D. et al. Resistivity phase diagram of cuprates revisited. *Phys. Rev. B* **102**, 075114 (2020).
30. Kovtun, P. K., Son, D. T. & Starinets, A. O. Viscosity in strongly interacting quantum field theories from black hole physics. *Phys. Rev. Lett.* **94**, 111601 (2005).
31. Giraldo-Gallo, P. et al. Scale-invariant magnetoresistance in a cuprate superconductor. *Science* **361**, 479–481 (2018).
32. Peierls, R. On the theory of the magnetic change in resistance. *Ann. Phys.* **10**, 97–110 (1931).
33. Hayes, I. M. et al. Scaling between magnetic field and temperature in the high-temperature superconductor $\text{BaFe}_2(\text{As}_{1-x}\text{P}_x)_2$. *Nat. Phys.* **12**, 916–919 (2016).
34. Nakamae, S. et al. Electronic ground state of heavily overdoped nonsuperconducting $\text{La}_{2-x}\text{Sr}_x\text{CuO}_4$. *Phys. Rev. B* **68**, 100502 (2003).
35. Cooper, R. A. et al. Anomalous criticality in the electrical resistivity of $\text{La}_{2-x}\text{Sr}_x\text{CuO}_4$. *Science* **323**, 603–607 (2009).
36. Abdel-Jawad, M. et al. Anisotropic scattering and anomalous normal-state transport in a high-temperature superconductor. *Nat. Phys.* **2**, 821–825 (2006).
37. Proust, C., Boaknin, E., Hill, R. W., Taillefer, L. & Mackenzie, A. P. Heat transport in a strongly overdoped cuprate: Fermi liquid and a pure *d*-wave BCS superconductor. *Phys. Rev. Lett.* **89**, 147003 (2002).

Publisher's note Springer Nature remains neutral with regard to jurisdictional claims in published maps and institutional affiliations.

© The Author(s), under exclusive licence to Springer Nature Limited 2021

Methods

Samples and transport measurements

Single-crystal $\text{La}_{2-y}\text{Nd}_y\text{Sr}_x\text{CuO}_4$ (Nd-LSCO) was grown at the University of Texas at Austin using a travelling-float-zone technique, with a Nd content $y = 0.4$ and nominal Sr concentration $x = 0.25$. The hole concentration is $p = 0.24 \pm 0.005$ (for more details, see ref. ²⁰). The value of T_c , defined as the point of zero resistance, is $T_c = 11$ K. The pseudogap critical point in Nd-LSCO is at $p^* = 0.23$ (ref. ²⁰).

Resistivity measurements were performed in the 45-T hybrid magnet at the National High Magnetic Field Laboratory in Tallahassee, USA. The sample resistance was measured with a standard four-point contact geometry using a Stanford Research 830 Lock-In Amplifier. The samples were driven with a current of $I_{\text{RMS}} = 1$ mA from a Keithley 6221 Current Source. Temperature was stabilized to within ± 1 mK around the target temperature at each angle. The uncertainty of the absolute temperature due to thermometer magnetoresistance is approximately ± 1 K at both $T = 6$ K and $T = 12$ K (horizontal error bars in Figs. 2c, 3a, b), but negligible at $T = 20$ K and above.

At $p = 0.24$, the upper critical field of Nd-LSCO is 10 T for $\mathbf{B} \parallel c$ (ref. ²⁵). By applying a magnetic field of $B = 45$ T at both $T = 25$ K and $T = 20$ K, the sample remains in the normal state while rotating the field from $\mathbf{B} \parallel c$ to $\mathbf{B} \parallel a$. At $T = 12$ K and $T = 6$ K the $p = 0.24$ sample is in the normal state when $\mathbf{B} \parallel c$, but superconductivity onsets when the field is rotated towards $\mathbf{B} \parallel a$, as shown in Fig. 2a.

The polar angle θ between the crystalline c -axis and the magnetic field was changed in situ continuously from about -15° to about 110° using a single-axis rotator (Extended Data Fig. 1a). A voltage proportional to the angle was recorded with each angle sweep. The angle θ was calibrated by finding symmetric points in the resistivity and scaling the measured voltage such that the symmetric points lie at $\theta = 0^\circ$ and $\theta = 90^\circ$ (Extended Data Fig. 1b). This procedure resulted in an uncertainty in θ of $\pm 0.5^\circ$. The azimuthal angle ϕ was changed by placing the sample on top of G-10 wedges machined at different angles: 15° , 30° and 45° . An illustration of the sample mounted on the rotator stage, with a G-10 wedge to set the azimuthal angle to be 30° , is shown in Extended Data Fig. 1. The samples and wedges were aligned under a microscope by eye to an accuracy in ϕ of $\pm 2^\circ$.

Fitting method

Genetic algorithm. Computing the conductivity as described above involves free parameters (for example, t' , t'' , t_z , μ , τ_{iso} , τ_{aniso} , ν , defined below), which can be written as a vector \mathbf{x} . The optimal \mathbf{x} , which we refer to as \mathbf{x}^* , minimizes the chi-square (χ^2) statistic between the resistivity from the model $\rho_{zz}^{\text{model}}(\mathbf{x}, \theta, \phi)$ and the measured resistivity $\rho_{zz}^{\text{data}}(\theta, \phi)$ at all magnetic field orientations (θ, ϕ) :

$$\chi^2(\mathbf{x}) = \sum_{(\theta, \phi)} \left(\rho_{zz}^{\text{model}}(\mathbf{x}, \theta, \phi) - \rho_{zz}^{\text{data}}(\theta, \phi) \right)^2, \quad (3)$$

We thus seek \mathbf{x}^* such that:

$$\mathbf{x}^* = \arg \min_{\mathbf{x}} \chi^2(\mathbf{x}). \quad (4)$$

Using the Chambers formula to fit the ADMR measurements can be tricky for standard optimization algorithms such as gradient-based methods. They are either slow to converge, highly sensitive to the initial conditions or they tend to get stuck in local minima of the $\chi(\mathbf{x})$ landscape. That is the reason why we turned to a genetic algorithm (or 'differential evolution') as a global optimization method, which can avoid these issues. The genetic algorithm has become a standard fitting routine in science and it is carefully detailed in the supplementary information of ref. ³⁸. For this study, we used the differential evolution algorithm from the Python package `Imfit`³⁹ and our own C++ implementation. We back checked the efficiency of the

genetic algorithm with two other global optimizers, such as AMPGO (Adaptive Memory Programming for Global Optimization) and SHGO (Simplicial Homology Global Optimization) also made available in `Imfit`³⁹. The three optimizers all converged to the same results, confirming the robustness of our fit procedure.

Convergence criteria. The χ^2 values of each member of the population are calculated after each generation of optimization. The distribution of all these χ^2 values follows a Gaussian-like distribution. The genetic algorithm stops when the standard deviation of this distribution has reached less than 1% of the mean value of the distribution.

Error bars. When the fit reaches \mathbf{x}^* (the best-fit values), the error bars are calculated for each parameter by the statistical procedure of calculating the Hessian matrix, which represents the second derivative of the fit quality χ^2 in regard to each parameter. The error bars in Extended Data Table 2 are calculated as the square root of the diagonal values of the covariance matrix (inverse of the Hessian matrix) evaluated at \mathbf{x}^* . More details are available on the website of the Python package `Imfit`³⁹.

Fitting procedure. To find the tight-binding and scattering-rate parameter values that best describe the Fermi surface of Nd-LSCO at $p = 0.24$ at all temperatures, we searched the parameter space using the following. (1) We fit the ADMR data at the four temperatures (6 K, 12 K, 20 K, 25 K) simultaneously with the genetic algorithm. All temperatures share the same tight-binding parameters during the optimization process, but the scattering-rate parameters ($1/\tau_{\text{iso}}$, $1/\tau_{\text{aniso}}$ and ν for the cosine model equation (7)) are unique for each temperature. (2) The search range of the genetic algorithm for the tight-binding parameters was set at $\pm 30\%$ around the ARPES values provided by Johan Chang through private communications for the data presented in ref. ⁷: $\mu = -0.93t$, $t' = -0.136t$, $t'' = 0.068t$ and $t_z = 0.07t$ (this last value comes from ref. ²⁴ for Eu-LSCO, which shows identical atomic structure and electronic properties). Only $t = 190$ meV was kept fixed. (3) The absolute value of ρ_{zz} at each temperature—not just the relative change with angle—was included in the optimization.

Band structure

We use a three-dimensional tight-binding model of the Fermi surface that accounts for the body-centred tetragonal crystal structure of Nd-LSCO²⁴,

$$\begin{aligned} \varepsilon(k_x, k_y, k_z) = & -\mu - 2t[\cos(k_x a) + \cos(k_y a)] \\ & - 4t' \cos(k_x a) \cos(k_y a) \\ & - 2t'' [\cos(2k_x a) + \cos(2k_y a)] \\ & - 2t_z \cos(k_x a/2) \cos(k_y a/2) \cos(k_z c/2) \\ & \times [\cos(k_x a) - \cos(k_y a)]^2, \end{aligned} \quad (5)$$

where μ is the chemical potential, t , t' and t'' are the first-, second- and third nearest-neighbour hopping parameters, t_z is the interlayer hopping parameter, $a = 3.75$ Å is the in-plane lattice constant of Nd-LSCO, and $c/2 = 6.6$ Å is the CuO_2 layer spacing. The interlayer hopping has the form factor $\cos(k_x a/2) \cos(k_y a/2) [\cos(k_x a) - \cos(k_y a)]^2$, which accounts for the offset copper oxide planes between layers of the body-centred tetragonal structure⁴⁰.

The fit results of the ADMR data are presented in Fig. 2a, Extended Data Table 1 (for the tight-binding values) and Extended Data Table 2 (for the scattering-rate values). Although the genetic algorithm was allowed to search over a wide range of parameters, we found that the optimal solution converged towards t' , t'' and t_z values extremely close to the ARPES values, with a 7% deviation at most for t_z . Only μ , and therefore the doping p , is substantially different from the

ARPES value. The higher doping found by ARPES may be due to the difficulty in accounting for the k_z dispersion, or may be due to different doping at the surface. Nevertheless, the shape of the Fermi surface found by fitting the ADMR data (Fig. 1d) is electron like and qualitatively identical to the one measured by ARPES⁷, and the doping we find ($p = 0.248$) is very close to the nominal one $p = 0.24 \pm 0.005$ (ref. 6).

This demonstrates that the Fermi surface is correctly mapped out by the ADMR data. In the figures and the analysis presented in this paper, we use the tight-binding values from Extended Data Table 1, and for simplicity we refer to them as the ‘tight-binding values from ARPES’, as they only differ by the chemical potential value.

Determining the energy scale t

Fitting ADMR to a tight-binding model using Boltzmann transport determines the relative variation between the different tight-binding parameters. The overall scale t , however, must be determined independently. Although ARPES can determine t by fitting the measured dispersion to a tight-binding model, ARPES does not necessarily have the sensitivity to determine all band renormalizations at the Fermi energy. As electrical transport is only sensitive to renormalizations at the Fermi energy, and not to the overall bandwidth, it is crucial to determine t accurately if one is to quantitatively determine the scattering rate. The experimentally determined quantity that is most sensitive to band renormalizations near the Fermi energy is the specific heat, which is sensitive to the total density of states. To determine t , we calculate the density of states from our tight-binding model and adjust t to match the experimentally determined electronic specific heat, C_{el} .

In Extended Data Fig. 2a, we compare the calculated Sommerfeld coefficient $\gamma \equiv C_{el}/T$ to the measured electronic specific heat for Nd-LSCO. At $p = 0.27$, $p = 0.36$ and $p = 0.40$, C_{el}/T is found to be constant at low T , with $\gamma = 11 \pm 1 \text{ mJ K}^{-2} \text{ mol}^{-1}$, $\gamma = 6.5 \pm 1 \text{ mJ K}^{-2} \text{ mol}^{-1}$ and $\gamma = 5.5 \pm 1 \text{ mJ K}^{-2} \text{ mol}^{-1}$, respectively (Extended Data Fig. 2b)²⁵. For Nd-LSCO at $p = 0.24$, Michon et al.²⁵ report a $\log(1/T)$ increase in the specific heat below 10 K. Above 10 K, this increase must terminate to be consistent with the specific heat at $p = 0.27$, as the specific heat generally decreases with increased doping as the band moves away from the van Hove points, and the mass enhancement decreases away from p^* . The difference between the measured specific heat at 6 K and the lower bound set by the $p = 0.27$ data are 20%. As the origin of the $\log(1/T)$ increase is unknown, and its effect on the electrical transport is unclear, we take the density of states across our temperature range—from 6 K to 25 K—to be constant. We know of at least two cases where the quasiparticle effective mass m^* is independent of temperature in a metal that does exhibit T -linear resistivity. The first case is the electron-doped cuprates, where the mass from quantum oscillations in $\text{Nd}_{2-x}\text{Ce}_x\text{CuO}_4$ (NCCO) at $x = 0.17$ obeys the standard Lifshitz–Kosevich form, with a constant mass of $m^* = 2.3m_e$, where m_e is the bare electron mass (ref. 41). Over the same temperature range, the resistivity of $\text{Pr}_{2-x}\text{Ce}_x\text{CuO}_4$ (PCCO) at $x = 0.17$ is purely T -linear⁴². The second case is Tl2201 at $p = 0.30$, where quantum oscillations are perfectly Lifshitz–Kosevich-like, indicating a constant m^* (ref. 43). Over the same temperature range where the quantum oscillations are measured, from 1 K to 5 K, the resistivity of Tl2201 is dominated by the T -linear component³⁷. Thus, there is no clear link between $\log(1/T)$ specific heat and T -linear resistivity.

We therefore take a value of $t = 130 \text{ meV}$ as a lower bound on t (Extended Data Fig. 2a). The upper bound on t is set by ARPES, because ARPES is not necessarily sensitive to all low-energy renormalizations near the Fermi energy. This upper bound is $t = 190 \text{ meV}$ (ref. 24). Extended Data Fig. 2a shows that a value of $t = 160 \pm 30 \text{ meV}$ —encompassing the lower bound set by specific heat and the upper bound set by ARPES—agrees well with the measured specific heat across the entire doping range, passing through all error bars, from $p = 0.23$ to $p = 0.40$.

The fractional reduction in bandwidth from the ARPES value, that is, $t(\text{ARPES})/t(\gamma)$, is 1.2.

Scattering-rate models

To eliminate a possible model dependence of the scattering rate to best describe the ADMR data of Nd-LSCO at $p = 0.24$, we tested different scattering-rate models that we detail below.

Isotropic scattering rate. We first consider a constant scattering-rate model

$$1/\tau = 1/\tau_{\text{iso}}, \quad (6)$$

where $1/\tau_{\text{iso}}$ is the amplitude of the isotropic scattering rate. With this, we try to fit the ADMR data of Nd-LSCO at $p = 0.24$. The best-fit result is shown in Extended Data Fig. 3b, which demonstrates that a constant scattering-rate model fails to reproduce the data. Instead, the signal increases monotonically out to $\theta = 90^\circ$. The features at $\theta = 40^\circ$ and $\theta = 90^\circ$ are present—as they reflect the topology of the Fermi surface—but come with wrong amplitudes and proportions in respect to each other. Using a smaller or higher scattering rate just changes the overall amplitude of the curve, but not the proportions of the features in respect to each other.

Cosine anisotropic scattering rate. We next consider the most minimalistic anisotropic scattering-rate model, one based on a cosine function:

$$1/\tau(\phi) = 1/\tau_{\text{iso}} + 1/\tau_{\text{aniso}} |\cos(2\phi)|^v, \quad (7)$$

where $1/\tau_{\text{iso}}$ is the amplitude of the isotropic scattering rate, $1/\tau_{\text{aniso}}$ is the amplitude of the ϕ -dependent scattering rate and v is an integer. The best fit using this model is plotted in Fig. 2a and Extended Data Fig. 3c, and parameter values are listed in Extended Data Table 2. The features at $\theta = 40^\circ$ and $\theta = 90^\circ$ are now present with the same amplitudes as the data. With as few parameters as possible, this model captures the trend of the anti-nodal regions of the Fermi surface to have shorter quasiparticle lifetimes in the cuprates^{27,44}, particularly close the van Hove singularity at $p \approx 0.23$. This is the model we used in Fig. 2—it should be seen as the simplest phenomenological model able to capture the correct shape of the real scattering rate, with the least number of free parameters.

Polynomial and tanh anisotropic scattering rates. To ensure that the cosine model captures the phenomenology of the real scattering rate without being a ‘fine-tuned’ model, we now turn to two other anisotropic scattering-rate models based on entirely different functions. The first model incorporates a hyperbolic tangent function (equation (8)) and the second is a polynomial function (equation (9)); the most ‘adaptive’ of the three models). The ‘tanh’ model

$$1/\tau(\phi) = \frac{1/\tau_{\text{iso}}}{|\tanh(a_1 + a_2 |\cos(2(\phi + \pi/4))|^{a_3})|}, \quad (8)$$

and the polynomial model

$$1/\tau(\phi) = 1/\tau_{\text{iso}} + |a_1\phi + a_2\phi^2 + a_3\phi^3 + a_4\phi^4 + a_5\phi^5|, \quad (9)$$

with $\phi(\text{mod } \pi/4) \in [0, \pi/4]$.

The best fits for these two models are plotted in Extended Data Fig. 3e, f. The entire temperature dependence and the transport coefficients calculated with the ‘tanh’ model are shown in Extended Data Fig. 4. The fits are not significantly different from the ‘cosine’ model—slightly more refined—which demonstrates that the essential physics is captured by the minimalistic cosine model. Extended Data Fig. 3d

shows that the three anisotropic models all give the same ϕ -dependence close to the nodes at $\theta = 45^\circ$ and have the same slopes near $\theta = 90^\circ$. The models differ in their absolute values of the scattering rate near $\theta = 90^\circ$: we attribute this small discrepancy to the fact that the scattering rate at $\theta = 90^\circ$ is so high that a small change in curvature in the model can make the value at $\theta = 90^\circ$ vary. Nonetheless, this is just a quantitative difference, as the transport coefficients calculated remain similar, the anisotropic component of the scattering rate remains temperature independent and the isotropic part is T -linear for both the ‘cosine’ and ‘tanh’ models as shown in Extended Data Fig. 4b. We do not present the temperature dependence of the ‘polynomial’ model because of the long time it takes to converge with many more parameters.

ADMR for $B = 35$ T

In Extended Data Fig. 5a, we show ADMR data measured at $B = 35$ T. Owing to the smaller magnetic field, the data are very different from those taken at $B = 45$ T, in terms of both the magnitude of the ADMR and the qualitative features.

By following the same fitting procedure at $B = 35$ T, in Extended Data Fig. 5b we show that we obtain scattering rates and tight-binding parameters that are the same to within 1% of those that describe the data at $B = 45$ T—the only parameter that changes between the two sets of fits is the magnetic field.

This shows that our scattering rate and tight-binding parameters are robust and do not rely on fine-tuning parameters to match the data at $B = 45$ T. Moreover, this shows that the scattering rate does not depend on field, and that all magnetoresistance arises from the orbital motion of electrons under the Lorentz force.

Data availability

The experimental data presented in this paper are available at <http://wrap.warwick.ac.uk/152398/>. The results of the conductivity simulations are available from the corresponding authors upon reasonable request.

Code availability

The code used to compute the conductivity is available from the corresponding authors upon reasonable request.

38. Ramshaw, B. J. et al. Broken rotational symmetry on the Fermi surface of a high- T_c superconductor. *npj Quantum Mater.* **2**, 8 (2017).
39. Newville, M., Stensitzki, T., Allen, D. B. & Ingargiola, A. LMFIT: non-linear least-square minimization and curve-fitting for python. *Zenodo* <https://zenodo.org/record/11813#.YNRimOhKhPY> (2014).
40. Chakravarty, S., Sudbø, A., Anderson, P. W. & Strong, S. Interlayer tunneling and gap anisotropy in high-temperature superconductors. *Science* **261**, 337–340 (1993).
41. Helm, T. *Electronic Properties of Electron-Doped Cuprate Superconductors Probed by High-Field Magnetotransport*. PhD thesis, Technical Univ. Munich (2013).
42. Fournier, P. et al. Insulator–metal crossover near optimal doping in $\text{Pr}_{2-x}\text{Ce}_x\text{CuO}_4$: anomalous normal-state low temperature resistivity. *Phys. Rev. Lett.* **81**, 4720–4723 (1998).
43. Bangura, A. F. et al. Fermi surface and electronic homogeneity of the overdoped cuprate superconductor $\text{Tl}_2\text{Ba}_2\text{CuO}_{6-\delta}$ as revealed by quantum oscillations. *Phys. Rev. B* **82**, 140501 (2010).
44. Analytis, J. G., Abdel-Jawad, M., Balicas, L., French, M. M. J. & Hussey, N. E. Angle-dependent magnetoresistance measurements in $\text{Tl}_2\text{Ba}_2\text{CuO}_{6-\delta}$ and the need for anisotropic scattering. *Phys. Rev. B* **76**, 104523 (2007).

Acknowledgements We acknowledge helpful discussions with J. Analytis, D. Chowdhury, N. Doiron-Leyraud, N. Hussey, M. Kartsovnik, S. Kivelson, D.-H. Lee, P. A. Lee, S. Lewin, A. Maharaj, K. Modic, C. Murthy, S. Musser, C. Proust, S. Sachdev, A. Shekhter, S. Todadri, A.-M. Tremblay and C. Varma. A portion of this work was performed at the National High Magnetic Field Laboratory, which is supported by the National Science Foundation Cooperative Agreement No. DMR-1644779 and the State of Florida. P.A.G. acknowledges that this project is supported by the European Research Council (ERC) under the European Union’s Horizon 2020 research and innovation programme (Grant Agreement No. 681260). J.-S.Z. was supported by an NSF grant (MRSEC DMR-1720595). L.T. acknowledges support from the Canadian Institute for Advanced Research (CIFAR) as a Fellow and funding from the Natural Sciences and Engineering Research Council of Canada (NSERC; PIN: 123817), the Fonds de recherche en recherche du Québec - Nature et Technologies (FRQNT), the Canada Foundation for Innovation (CFI) and a Canada Research Chair. This research was undertaken thanks in part to funding from the Canada First Research Excellence Fund. Part of this work was funded by the Gordon and Betty Moore Foundation’s EPIQS Initiative (Grant GBMF5306 to L.T.) B.J.R. and Y.F. acknowledge funding from the National Science Foundation under grant no. DMR-1752784.

Author contributions A.L., P.A.G., L.T. and B.J.R. conceived the experiment. J.Z. grew the sample. A.L., F.L. and C.C. performed the sample preparation and characterization. G.G., Y.F., A.L., D.G., P.A.G. and B.J.R. performed the ADMR measurements at the National High Magnetic Field Laboratory in Tallahassee. G.G., Y.F., S.V. and B.J.R. performed the data analysis and simulations. G.G., L.T. and B.J.R. wrote the manuscript with input from all other co-authors. L.T. and B.J.R. supervised the project.

Competing interests The authors declare no competing interests.

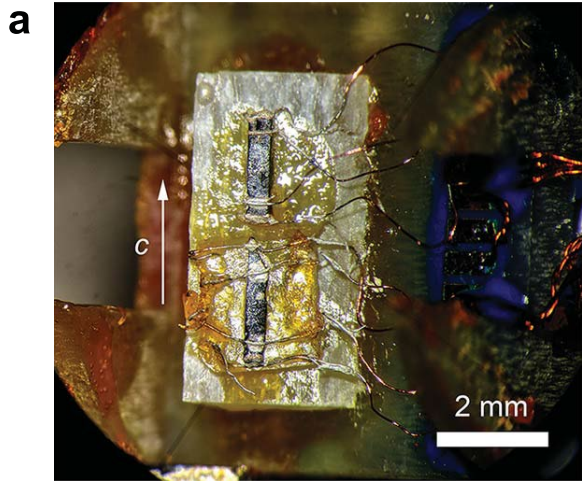
Additional information

Supplementary information The online version contains supplementary material available at <https://doi.org/10.1038/s41586-021-03697-8>.

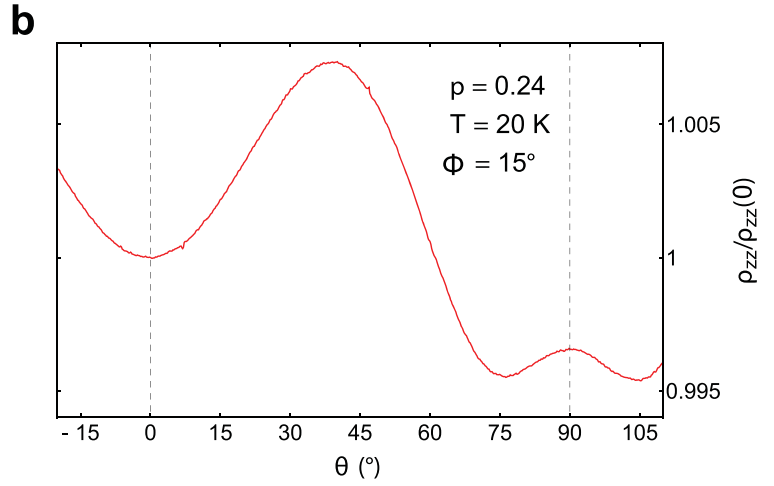
Correspondence and requests for materials should be addressed to L.T. or B.J.R.

Peer review information *Nature* thanks Antoine Georges and the other, anonymous, reviewer(s) for their contribution to the peer review of this work.

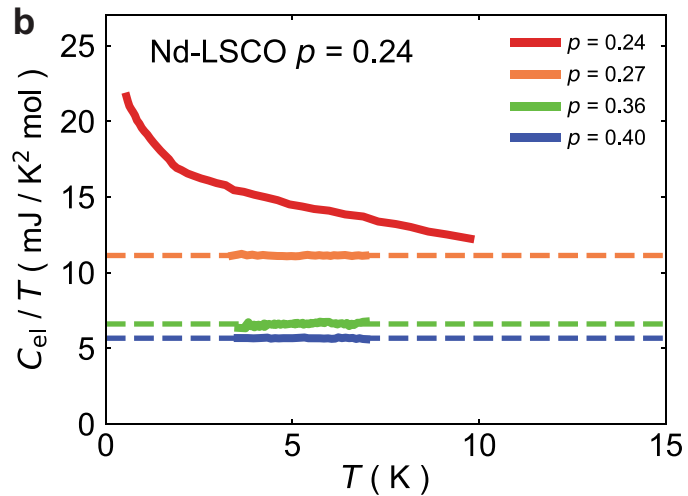
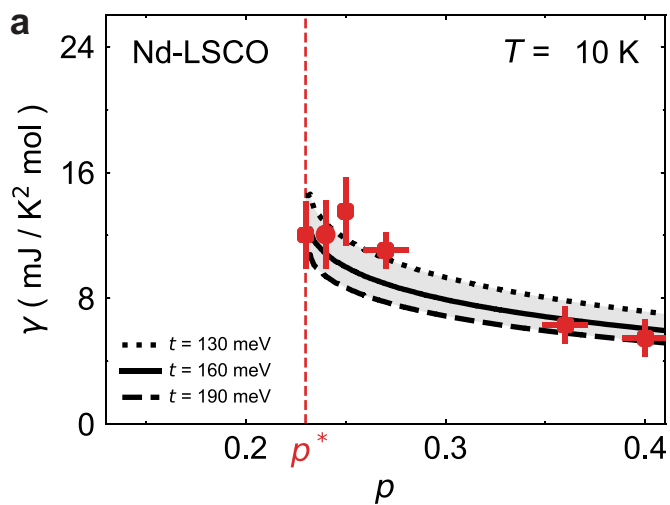
Reprints and permissions information is available at <http://www.nature.com/reprints>.



Extended Data Fig. 1 | ADMR experimental set up. a, A photograph of the sample on the rotator. The two samples here are mounted on a G-10 wedge to provide an azimuthal angle ϕ of 30° . Additional wedges provided angles of

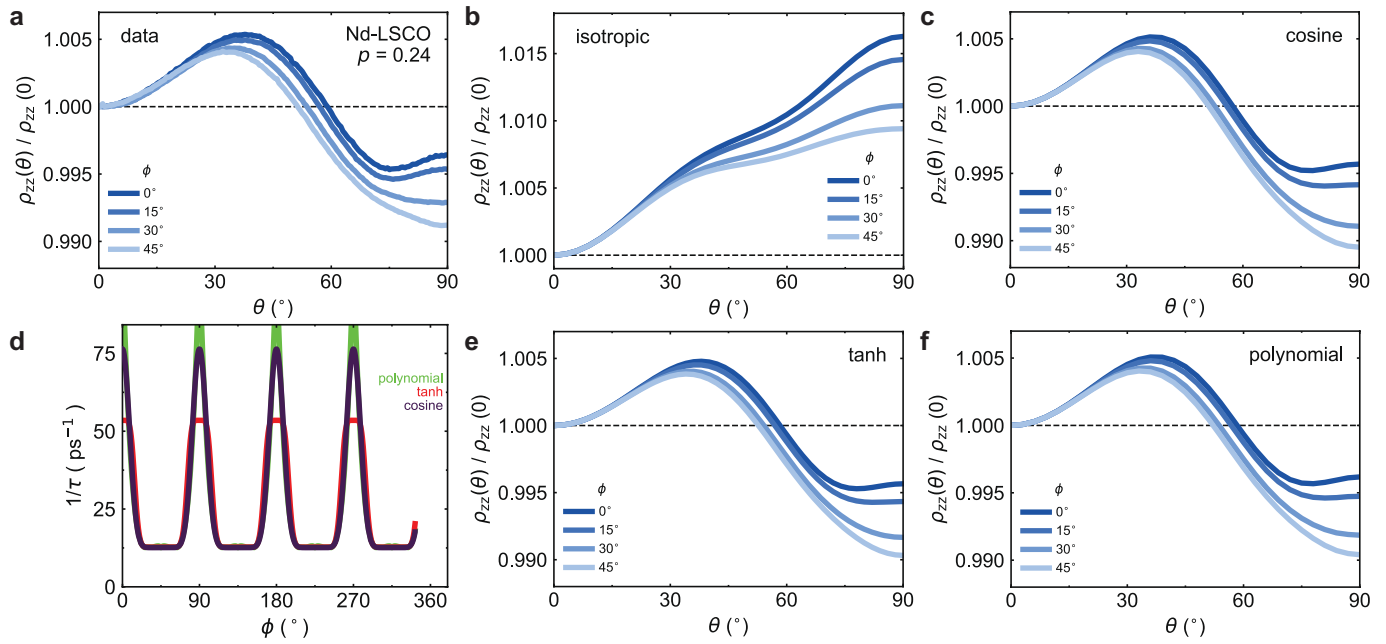


$\phi = 15^\circ$ and $\phi = 45^\circ$. **b**, ADMR as a function of θ angle from -15° to 110° and $\phi = 0$ at $T = 20 \text{ K}$ for Nd-LSCO $p = 0.24$, showing the symmetry of the data about these two angles.



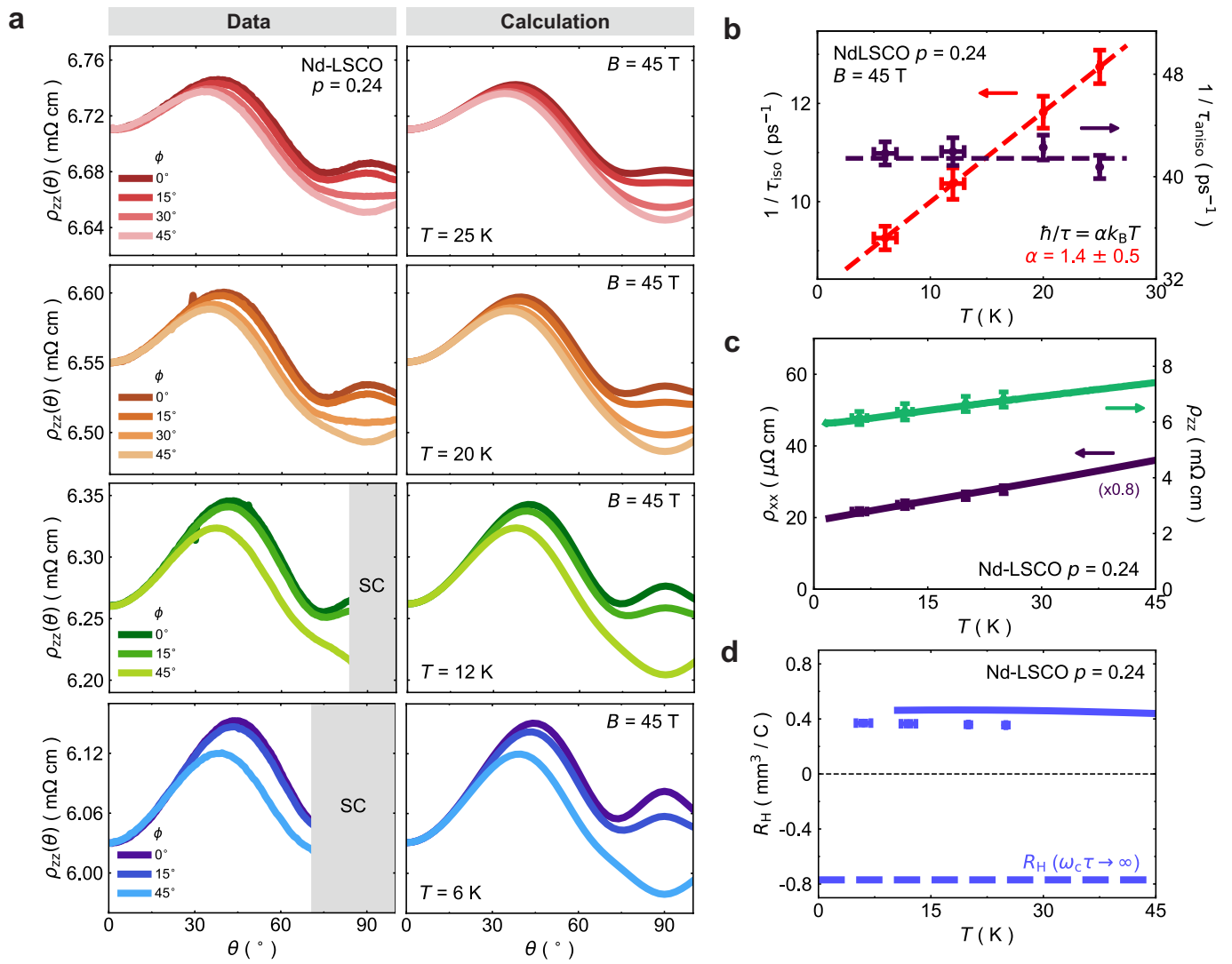
Extended Data Fig. 2 | Calculated and measured Sommerfeld coefficients of Nd-LSCO. **a**, The Sommerfeld coefficient γ for Nd-LSCO as a function of doping. The measured values (red circles) are obtained from measurements of the electronic specific heat C_{el}/T at $T = 10$ K (ref. ²⁵). For the calculated γ (black dashed, dotted and solid lines), we use the tight-binding parameters from our

ADMR analysis for three different values of t , as indicated. The grey band represents the region of consistency between the calculations and the data. **b**, Electronic specific heat C_{el}/T as a function of temperature for Nd-LSCO $p = 0.24, 0.27, 0.36$ and 0.40 (ref. ²⁵). The data are the solid lines and the dashed lines represent extrapolations.

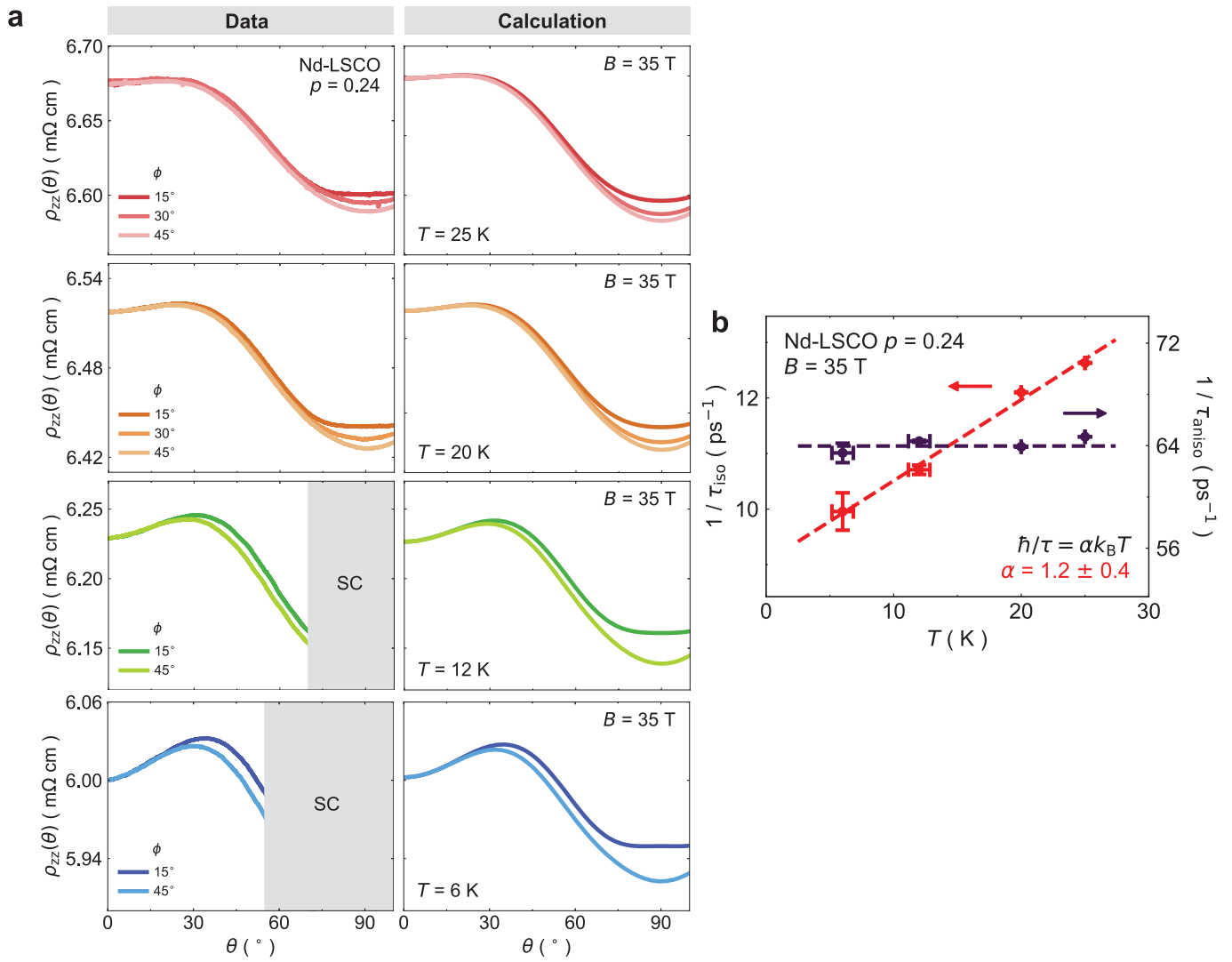


Extended Data Fig. 3 | Fit of the Nd-LSCO $\rho = 0.24$ data with different scattering-rate models. **a**, ADMR data on Nd-LSCO $\rho = 0.24$ at $T = 25$ K and $B = 45$ T. **b, c, e, f**, Best fits for the ADMR data in **a** using the Fermi surface in Fig. 1d and an isotropic scattering-rate model (**b**), and three different

anisotropic scattering-rate models: cosine (**c**), tanh (**e**) and polynomial (**f**). **d**, The three different anisotropic scattering rates as a function of the azimuthal angle ϕ at $T = 25$ K.



Extended Data Fig. 4 | ADMR and quasiparticle scattering rate of Nd-LSCO at $p = 0.24$ for the tanh model. This figure is the same as Figs. 2a, 3a, b, except that the ADMR has been fitted using the tanh model instead of the cosine model (Extended Data Fig. 3).



Extended Data Fig. 5 | ADMR and quasiparticle scattering rate of Nd-LSCO at $p = 0.24$ for $B = 35$ T. **a, **b**.** This figure is the same as Fig. 2a, c except that the ADMR data are taken at $B = 35$ T (**a**). The fit has been carried out using the cosine

model. **b** shows that scattering-rate values are identical to within a percent of those obtained from the fit to the data at $B = 45$ T, shown in Fig. 2c.

Extended Data Table 1 | Tight-binding parameters from the fit to the ADMR data at $p = 0.24$

	t (meV)	t'/t	t''/t	t_z/t	μ/t	p
ADMR	160 ± 30	-0.1364 ± 0.0005	0.0682 ± 0.0005	0.0651 ± 0.0005	-0.8243 ± 0.0005	0.248
ARPES	190	-0.136	0.068	0.07		0.28

Best-fit tight-binding values for the Nd-LSCO $p = 0.24$ ADMR data (using the cosine scattering-rate model of equation (7)). The hopping parameter $t = 160 \pm 30$ meV was fixed by the measured specific heat: see the section 'Determining the energy scale t' ' for more information. The results are extremely close to ARPES tight-binding values reported in Matt et al.⁷ and Horio et al.²⁴, reproduced here on the second line. Error bars on the ADMR-derived values were obtained following the procedure described in Methods. The error bar on the value of t_z measured by ARPES is $\pm 0.02t$ (J. Chang and M. Horio, private communication).

Extended Data Table 2 | Results of the fit of the Nd-LSCO $p = 0.24$ data with the cosine scattering-rate model

T (K)	$1/\tau_{\text{iso}}$ (ps^{-1})	$1/\tau_{\text{aniso}}$ (ps^{-1})	ν	t (meV)	t'	t''	t_z	μ	p
25	12.595 ± 0.002	63.823 ± 0.257	12 ± 1	160 ± 30	$-0.1364t$	$0.0682t$	$0.0651t$	$-0.8243t$	0.248
20	11.937 ± 0.003	63.565 ± 0.759	12 ± 1	160 ± 30	$-0.1364t$	$0.0682t$	$0.0651t$	$-0.8243t$	0.248
12	10.663 ± 0.005	63.599 ± 0.235	12 ± 1	160 ± 30	$-0.1364t$	$0.0682t$	$0.0651t$	$-0.8243t$	0.248
6	9.628 ± 0.049	63.929 ± 0.902	12 ± 1	160 ± 30	$-0.1364t$	$0.0682t$	$0.0651t$	$-0.8243t$	0.248

Best-fit scattering rate and tight-binding values of the Nd-LSCO $p = 0.24$ ADMR data plotted in Fig. 2a. The fit was achieved by the multi-temperature fit procedure described in the Methods section. Error bars on the scattering-rate parameters were obtained following the procedure described in the 'Fitting method' section. Error bars on the tight-binding parameters are all $\pm 0.0005t$.